

1 **A satellite observation-based analysis of cirrus ice**  
2 **crystal number concentrations and underlying cirrus**  
3 **formation mechanisms**

4  
5 **Kai Wang<sup>1</sup>, Xiaocong Wang<sup>2</sup>, Qianshan He<sup>3</sup>, Hong Nie<sup>4</sup>, Yanyu**  
6 **Wang<sup>5</sup>, and Yonghang Chen<sup>6</sup>**

7 <sup>1</sup>College of Atmospheric Science, Nanjing University of Information Science and  
8 Technology, Nanjing, China

9 <sup>2</sup>Institute of Atmospheric Physics, Chinese Academy of Sciences, Beijing, China

10 <sup>3</sup>Shanghai Meteorological Bureau, Shanghai, China

11 <sup>4</sup>Qinghai Meteorological Service Centre, Xining, China

12 <sup>5</sup>State Environmental Protection Key Laboratory of Formation and Prevention of  
13 Urban Air Pollution Complex, Shanghai Academy of Environmental Sciences,  
14 Shanghai, China

15 <sup>6</sup>College of Environmental Science and Engineering, Donghua University, Shanghai,  
16 China

17 Correspondence to: Qianshan He (oxeye75@163.com)

18  
19 **Abstract.**

20 Cirrus clouds typically form in the upper troposphere and play an important role in the  
21 Earth's energy balance and the atmospheric water cycle. This study utilizes  
22 DARDAR-Nice data within June to August from 2006 to 2016 (except 2011),  
23 combined with CloudSat cloud products and other related aerosol products, to analyze  
24 the distribution characteristics and some possible formation mechanisms of ice crystal  
25 number concentration ( $N_i$ ) in cirrus clouds over the Tibetan Plateau (TP). The results  
26 indicate that  $N_i$  over the northern TP is generally lower than that over the southern TP.  
27 This contrast shows a certain connection with differences in aerosol occurrence and  
28 the intensity of convective activity between the two regions. The vertical distribution  
29 of  $N_i$  over the TP exhibits a characteristic V-shaped structure, which is dominated by  
30 homogeneous freezing. When deep convective activity occurs,  $N_i$  tends to increase at

1 the same altitude compared to non-convective conditions. In contrast, under dust- and  
2 smoke-influenced conditions,  $N_i$  is generally lower, which may be related to ice  
3 formation via heterogeneous nucleation. In addition, weak vertical motion near 400  
4 hPa over the northern TP is linked to an earlier appearance of the  $N_i$  peak at altitudes  
5 below the homogeneous freezing threshold temperature ( $-38\text{ }^\circ\text{C}$ ).

## 6 7 **1 Introduction**

8 Cloud is the key link in the energy and water vapor balance of the  
9 earth-atmosphere system and plays an important role in global weather and climate  
10 change (Wang and Zhao, 1994; Stephens, 2005). Cirrus clouds are composed of a  
11 large number of non-spherical ice crystal particles with a wide range coverage of  
12 Earth surface (Guignard et al., 2011; Baran, 2012), which can reflect solar short-wave  
13 radiation and absorb terrestrial long-wave radiation, affect the energy balance of the  
14 upper troposphere and stratosphere and play an important role in the global water  
15 cycle and climate change (Kienast-Sjögren et al., 2016). A definite knowledge of  
16 cirrus microphysical properties and their formation mechanism is an important  
17 prerequisite for deepening the understanding of global climate change.

18 The Tibetan Plateau (TP) is a highest and largest plateau of the world, known as  
19 the 'roof of the world', affects significantly the climate patterns in eastern and  
20 southwestern China, and even global, as well as the global water circulation system,  
21 due to the unique dynamic and thermal effects. In summer, South Asian high controls  
22 the TP, where the cirrus clouds show different characteristics from that in other  
23 regions along the same latitude. On the one hand, the TP and its southern slope serves  
24 as an important windows for troposphere-stratosphere material exchange, where the  
25 frequent deep convective activities in summer have transported water vapor and  
26 anthropogenic aerosol pollutants to the upper troposphere-lower stratosphere (UTLS)  
27 (Fu et al., 2006; Randel et al., 2010; Chen et al., 2019). On the other hand, the  
28 substantial elevation difference over the southern part of the TP and the topographic  
29 uplift movement promote warm and humid air mass rising into the upper troposphere,  
30 which is conducive to the occurrence and development of cirrus clouds (Zhao et al.,  
31 2019; Yang et al., 2020). Also, the accumulation of aerosols is conducive to the  
32 formation of cirrus ice crystals by heterogeneous nucleation.

1        So far, the study on cirrus clouds over the TP mainly focused on the  
2 spatiotemporal variation characteristics, cloud height, and cirrus cloud formation  
3 mechanism. Xue et al. (2018) found that the occurrence frequency, average effective  
4 radius of ice particles and cloud top height reached the maximum in summer over the  
5 TP using Moderate-Resolution Imaging Spectroradiometer (MODIS). Gao et al. (2003)  
6 found that the occurrence frequency of cirrus clouds reached a maximum in April and  
7 a minimum in November by MODIS data. Chen and Liu (2005) found that the  
8 occurrence of cirrus clouds over the TP in March and April was closely related to the  
9 slow uplift of warm and humid air mass to the tropopause due to topographic effect. Li  
10 et al. (2005) found that deep convection activities affected by Asian Summer  
11 Monsoon (ASM) were closely related to cirrus cloud formation over the TP using  
12 satellite observations. Zhang et al. (2020) used Cloud-Aerosol Lidar and Infrared  
13 Pathfinder Satellite Observations (CALIPSO) to investigate the generation  
14 mechanism of plateau cirrus clouds, revealing that large-scale orographic uplift,  
15 temperature fluctuations, and deep convection play crucial roles in their formation.

16        Previous studies have shown that the formation of cirrus ice crystals is primarily  
17 governed by three mechanisms: deep convective cloud anvil overflow (Prabhakara et  
18 al., 1993; Wang et al., 1996), homogeneous nucleation and heterogeneous nucleation  
19 (Wang et al., 1997; Chen et al., 2000; Cantrell and Heymsfield, 2005). Updrafts and  
20 strong horizontal currents in the upper troposphere induced by deep convective  
21 activities lead to rapidly spreading around into cloud anvils composed of ice crystal  
22 particles (Takahashi and Luo, 2012). The homogeneous freezing of supercooled water  
23 droplets or aqueous aerosol particles to form ice crystals requires temperatures below  
24 approximately  $-38^{\circ}\text{C}$  and sufficiently high ice supersaturation (Duft and Leisner,  
25 2004; Murray et al., 2010). While heterogeneous nucleation to form ice crystals  
26 requires relatively higher ambient temperature but insoluble aerosol particles (such as  
27 black carbon, dust) as ice-nucleating particles (INPs) (Morris et al., 2004; Murray et  
28 al., 2010; Shi et al., 2015; Fan et al., 2019).

29        Different formation mechanisms result in different effects on the microphysical  
30 characteristics of cirrus ice crystals, in which ice crystal number concentration ( $N_i$ )

1 plays a crucial role in understanding and characterizing cirrus clouds (Comstock et al.,  
2 2008).  $N_i$  is widely used as a key variable in cloud forecasting to predict cloud  
3 evolution and is potentially closely linked to aerosol concentrations, making it an  
4 important indicator for studying the impact of aerosols on ice cloud formation (Khain  
5 et al., 2000; Kay and Wood, 2008; Hendricks et al., 2011). However, current climate  
6 models and satellite observations face significant limitations in obtaining and utilizing  
7  $N_i$ , which can lead to substantial biases in simulating cloud microphysical processes,  
8 evaluating aerosol-cloud interactions, and calculating indirect radiative effects (Zhang  
9 et al., 2013; Sourdeval et al., 2018). It is generally recognized that homogeneous  
10 nucleation is the dominant mechanism determining  $N_i$  (Cantrell and Heymsfield,  
11 2005). When enough INPs occurs in the atmosphere, heterogeneous nucleation  
12 precedes homogeneous nucleation to form ice crystals, resulting in a consumption of a  
13 large amount of water vapor and a decrease in the ambient supersaturation.  
14 Suppressed homogeneous nucleation will further impede the increase in the  $N_i$  (Chen  
15 et al., 2000; Kärcher and Lohmann, 2003; Shi et al., 2017). In the region of less  
16 convective activities, the effective radius of ice particles increases with the increase of  
17 INPs. Jin et al. (2007) used a three-dimensional storm cloud model (IAP-CSM3D) to  
18 analyze the relation between convective activity and cirrus cloud, found that the  
19 number concentration of ice crystal formed by deep convective cloud anvil overflow  
20 decreases with a decrease in water vapor from the convective activity transports.

21 However, the 3D-distribution characteristics of  $N_i$  and the corresponding  
22 contribution from deep convective cloud anvil overflow, homogeneous nucleation and  
23 heterogeneous nucleation over the TP is not very clear. This study uses  
24 liDAR-raDAR-Number concentration of ICE particles (DARDAR-Nice) data to  
25 analyze the spatial distribution characteristics of medium-upper cirrus clouds in  
26 summer from 2006 to 2016 (except 2011), over the TP. The formation mechanism of  
27 ice particles also be explored in combination of CALIPSO satellite aerosol products  
28 with reanalysis data. Furthermore, this also sheds light on the role of aerosols in the  
29 upper atmosphere of the TP in the process of cirrus ice crystal formation. The results

1 will contribute to a deeper understanding of the thermodynamic effects of the TP and  
2 further improve the accuracy of climate simulations.

## 3 4 **2 Data and methods**

### 5 **2.1 Satellite observations**

6 This study uses ten summers (June-July-August, JJA) of multi-satellite  
7 observations during 2006 to 2016, except for 2011 due to data gaps, to investigate the  
8 distribution characteristics and formation mechanism of ice crystal particles over the  
9 TP. The primary dataset is the DARDAR-Nice product, complemented by additional  
10 retrievals from CloudSat and CALIPSO observations.

11 The DARDAR-Nice PRO product provides high-vertical-resolution estimates of  
12  $N_i$  retrieved along the A-Train satellite track. The retrievals are based on the VarCloud  
13 algorithm (Delanoë and Hogan, 2008; 2010), which combines observations from the  
14 Cloud Profiling Radar onboard CloudSat and the cloud-aerosol Lidar with Orthogonal  
15 Polarization (CALIOP) lidar on CALIPSO. DARDAR-Nice profiles are provided  
16 with a vertical resolution of 60 m. The product includes  $N_i$  values and corresponding  
17 uncertainty estimates for particle with size larger than 5, 25 and 100  $\mu\text{m}$ . In this study,  
18 the standard error of  $N_i$  is derived directly from the `icnc_5um_error` variable, ensuring  
19 that the uncertainty associated with each profile is properly represented in the analysis.  
20 This production has been systematically and comprehensively evaluated based on  
21 theoretical considerations and a large body of in situ observations (Sourdeval et al.,  
22 2018). However, it tends to overestimate ice crystal number concentrations in cloud  
23 parcels warmer than  $-30^\circ\text{C}$ , due to the assumption of a monomodal particle size  
24 distribution in the retrieval algorithm. To ensure the reliability of the results, this study  
25 focuses exclusively on clouds with temperatures below  $-30^\circ\text{C}$  and discusses the  $N_i$  of  
26 ice crystals with sizes larger than 5  $\mu\text{m}$ .

27 In addition, although ice water content (IWC) is also provided in the  
28 DARDAR-Nice product, it has not been specifically validated. Therefore, this study  
29 uses IWC data from the CloudSat 2B-CWC-RO product  
30 (<ftp://ftp.cloudsat.cira.colostate.edu/>), for which the retrieval quality and accuracy

1 have been discussed in detail by Austin et al. (2007, 2009). Besides 2B-CWC-RO, the  
2 CloudSat 2B-CLDCLASS-LIDAR product is employed, which classifies clouds into  
3 eight types across ten vertical layers with a horizontal resolution of  $2.5 \text{ km} \times 1.4 \text{ km}$ .  
4 Its classification algorithm integrates vertical and horizontal cloud structures,  
5 precipitation features, cloud temperature, and MODIS radiative measurements to  
6 enhance classification accuracy. These CloudSat products provide critical  
7 microphysical parameters and cloud classification necessary for understanding ice  
8 cloud properties.

9 CALIPSO can monitor the vertical distribution characteristics of clouds and  
10 aerosols, automatically identify aerosol types, and provide global aerosol horizontal  
11 distribution characteristics and vertical distribution information (Zheng et al., 2018).  
12 Liu et al. (2008) also conducted aerosol detection using CALIPSO, further confirming  
13 its effective aerosol detection capabilities.

14 Dust aerosols exhibit strong ice-nucleating activity and represent an important  
15 global source of INPs (Hoose and Möhler, 2012; Murray et al., 2012; Ladino Moreno  
16 et al., 2013). Meanwhile, sampling studies during biomass burning conducted by  
17 Prenni et al. (2012) and McCluskey et al. (2014) indicate that particles from biomass  
18 combustion constitute a significant regional source of INPs, particularly when other  
19 effective INPs are scarce. In addition, recent observational analyses by Mamouri et al.  
20 (2023) and Ansmann et al. (2025) suggest that smoke aerosols can exert a substantial  
21 influence on ice crystal formation at altitudes while temperatures fall below  $-30 \text{ }^\circ\text{C}$ .  
22 Therefore, this study primarily focuses on the role of dust and smoke aerosols. This  
23 study employs information from the Level-2 Version 5 kmCLay standard products of  
24 the CALIPSO satellite data spanning from 2006 to 2016 (except 2011) to assess the  
25 impact of dust and smoke aerosols on the formation of cirrus clouds.

26 In this study, both daytime and nighttime satellite observations are included, the  
27 aerosol information is used to characterize climatological, grid-cell-averaged aerosol  
28 occurrence rather than instantaneous cloud-aerosol collocation.

## 29 **2.2 Reanalysis Data**

30 To investigate atmospheric context for the satellite observations, this study

1 utilizes ERA5 reanalysis data from the European Centre for Medium-Range Weather  
 2 Forecasts (ECMWF). ERA5 provides hourly global data at a spatial resolution of  
 3  $0.25^\circ \times 0.25^\circ$  across 37 vertical pressure levels, covering the period from 1979 to  
 4 the present (Xie et al., 2021). The key variables used in this study are specific  
 5 humidity and vertical wind velocity from ERA5, as well as temperature from satellite  
 6 observations. Together, these three variables are essential for analyzing atmospheric  
 7 conditions related to cirrus cloud formation and deep convective vertical transport.

8

9 Table 1. Overview of the satellite datasets and data products used in this study

Source	Dataset	Variable	Duration
		icnc_5um	
DARDAR	DARDAR-Nice PRO	icnc_5um_error	
		temperature	
Cloudsat	2B-CWC-RO	ice water content	2006 - 2016 (except 2011)
	2B-CLDCLASS-LIDAR	Cloud type(deep convection)	
Calipso	Level-2 Version 5 kmCLay	Aerosol type(dust 、 smoke 、 clean)	
ERA5	Reanalysis	specific humidity	
		vertical wind velocity	

10

11

12 **2.3 Research Methods**

13 The focus area of this study is the TP and its surrounding regions, spanning from  
 14  $66^\circ\text{E}$  to  $106^\circ\text{E}$  and  $24^\circ\text{N}$  to  $40^\circ\text{N}$ . The original orbital data of the DARDAR-Nice  
 15 PRO product, 2B-CLDCLASS-LIDAR classification product and 2B-CWC-RO cloud  
 16 product are interpolated into grid point data with a resolution of  $2^\circ \times 2^\circ$  based on the  
 17 method outlined in Wang et al. (2023). The 2B-CLDCLASS-LIDAR deep convective  
 18 cloud product was used to quantify deep convection. For each grid cell and time  
 19 interval, the presence of one or more deep convective clouds was counted as a single

1 event, irrespective of the number of profiles exhibiting convection. These events were  
 2 then summed over all intervals to yield the total number of deep convection  
 3 occurrences per grid cell. For the investigation of  $N_i$ , statistical analysis was  
 4 conducted at intervals of 60 m, based on the vertical resolution of the DARDAR-Nice  
 5 PRO product. Data points with large uncertainties were set to NaN to minimize bias  
 6 in the statistics.

7 The horizontal distribution of  $N_i$  may be influenced by uneven sample  
 8 distribution resulting from the varying occurrence frequency of ice particles across  
 9 different layers. To address this, we normalized  $N_i$  for each grid during the ten  
 10 summer seasons over the TP, to obtain the horizontal distribution of  $N_i$  for cirrus  
 11 clouds. The normalization process is presented in Eq. (1):

$$12 \quad y = \frac{\sum_{i=1}^{Num} x_i}{\sum_{i=1}^{Num} m_i} \quad (1)$$

13 Where  $x_i$  is the sum of  $N_i$  where the temperature is below  $-30^\circ\text{C}$ .  $Num$  is the total  
 14 number of profiles included in the analysis.  $m_i$  is the effective layers within the  
 15 corresponding grid cell for which  $N_i$  is greater than 0.  $y$  is the normalized  $N_i$  in the  
 16 corresponding grid.

17 To compute the vertical distribution of  $N_i$ , each profile is analyzed layer by layer.  
 18 For each profile, if  $N_i$  is present in any layer, the profile is counted as 1; this count is  
 19 used for normalizing the total number of profiles. For each layer, the  $N_i$  from all  
 20 profiles are summed and then divided by the total number of counted profiles,  
 21 yielding the normalized  $N_i$  for that layer. The detailed calculation method is given in  
 22 Eq. (2):

$$23 \quad a_n = \frac{\sum_{i=1}^{Num} a_{i,n}}{\sum_{i=1}^{Num} C_i} \quad (2)$$

1        where  $\overline{a}_n$  represents the normalized  $N_i$  for layer  $n$ ,  $a_{i,j}$  is the  $N_i$  in layer  $n$  of  
2 profile  $i$ ,  $C_i$  is the profile count ( $C_i = 1$  if  $N_i$  is present in at least one layer of profile  $i$ ,  
3 and  $C_i = 0$  otherwise).

4        In the absence of INPs in the atmosphere, ice crystal formation occurs primarily  
5 through homogeneous nucleation. It is generally acknowledged that temperatures near  
6  $-38$  °C represent the threshold for homogeneous freezing of supercooled water  
7 droplets and aqueous aerosol particles under sufficiently high ice supersaturation  
8 (Duft and Leisner, 2004; Murray et al., 2010; Koop and Murray, 2016).. Traditionally,  
9 the identification of homogeneous nucleation has relied primarily on temperature  
10 thresholds. However, due to the continuous dynamic growth of ice particles through  
11 condensation, accurate simulation remains challenging. Moreover, classical  
12 nucleation theory suggests that ice formation under purely homogeneous freezing  
13 conditions is generally considered to be uncommon in the natural atmosphere (Maeda,  
14 2021).

15        A novel approach is proposed to identify homogeneous nucleation by leveraging  
16 aerosol classification data from the CALIPSO satellite over the TP during the summer  
17 from 2006 to 2016. Specifically, when aerosol types are classified as ‘clean’, it  
18 indicates a low concentration of INPs, favoring the dominance of homogeneous  
19 nucleation in ice crystal formation. Kim et al. (2018) performed a statistical analysis  
20 of different aerosol types in this product and found that ‘clean’ aerosols account for  
21 only about 1% of occurrences, representing background aerosol with very low  
22 concentration, which further supports the validity of this assumption. Grid points  
23 identified exclusively with ‘clean’ aerosol conditions are therefore considered to have  
24 undergone only homogeneous nucleation.

25        Although CALIPSO provides detailed vertical profiles of aerosols, this study  
26 does not explicitly use the height-resolved information. Instead, the aerosol  
27 occurrence is analyzed at the grid-cell level without distinguishing altitude. This  
28 approach is adopted for two main reasons. First, CALIPSO’s aerosol detection is most  
29 reliable in the lower troposphere, while its sensitivity decreases significantly at higher

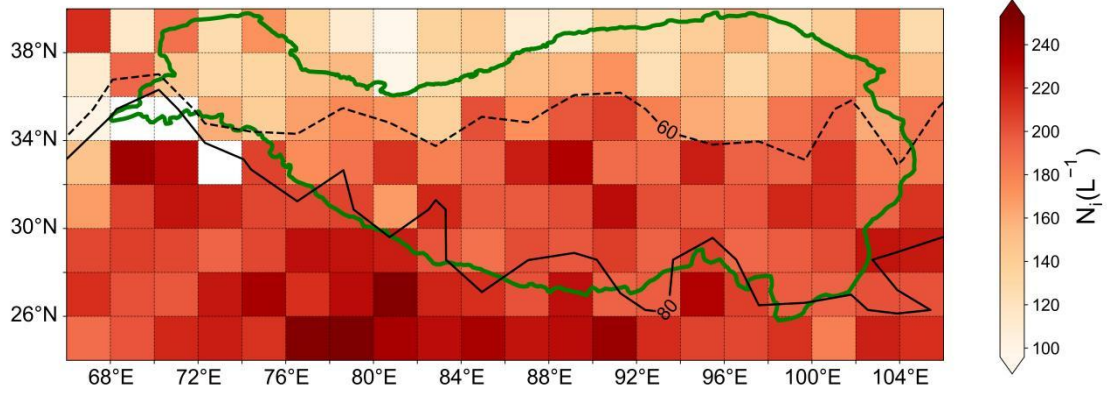
1 altitudes due to signal attenuation and the difficulty of distinguishing aerosols from  
2 thin cirrus clouds (Mao et al., 2022). Therefore, focusing on overall aerosol  
3 occurrence within each grid ensures better data consistency and avoids potential  
4 misclassification errors. Second, the  $N_i$  analyzed in this study corresponds to  
5 temperatures below  $-30^\circ\text{C}$ , the relevant aerosols are those that can influence cloud  
6 formation through vertical transport or large-scale dynamical processes, rather than  
7 being co-located at the same altitude. Hence, by integrating aerosol occurrence over  
8 the entire column within the same grid, the analysis effectively captures the overall  
9 influence of low-level dust or smoke aerosols on upper-tropospheric ice clouds,  
10 without introducing additional uncertainty from vertical matching. Therefore, the  
11 overall comparison, statistical results, and main conclusions remain robust.

12

### 13 **3 Results and Discussion**

#### 14 **3.1 Distribution characteristics of $N_i$ over the TP**

15 Based on the DARDAR-Nice PRO product, this study analyzes the spatial  
16 variation of  $N_i$  across all layers where the temperature is below  $-30^\circ\text{C}$  during the study  
17 period. The horizontal distribution of  $N_i$  in Fig. 1 demonstrates that the average  
18 concentration over the TP is  $187\text{ L}^{-1}$  during the study period. This value is higher than  
19 the approximately  $150\text{ L}^{-1}$  over the TP reported by Gryspeerdt et al. (2018), who used  
20 DARDAR-Nice data from 2006 to 2013 to study global  $N_i$  but focused only on  
21 cloud-top statistics. Considering that our analysis includes all layers below  $-30^\circ\text{C}$ , the  
22 higher  $N_i$  is reasonable and consistent with physical expectations, which also  
23 indirectly supports the reliability of our results. The average concentration in the  
24 south ( $24\text{-}30^\circ\text{N}$ ,  $66\text{-}106^\circ\text{E}$ ) is significantly higher than other areas, reaching  $213\text{ L}^{-1}$ ,  
25 with the maximum value located in the north-central region of India ( $24\text{-}26^\circ\text{N}$ ,  
26  $78\text{-}80^\circ\text{E}$ ), reaching  $253\text{ L}^{-1}$ . Over the north, including the Xinjiang, Inner Mongolia,  
27 the north of the Qilian Mountains and the Kunlun Mountains,  $N_i$  is only  $143\text{ L}^{-1}$ , only  
28 two-thirds of  $N_i$  compared with that in the southern region.



1  
2 **Fig. 1.** Horizontal distribution of the averaged  $N_i$  during the summer from 2006 to 2016 (except  
3 2011) over the TP. The green line is the border of the TP. The black solid lines represent the  
4 standard error of  $80 \text{ L}^{-1}$  and the black dotted line represents the value of  $60 \text{ L}^{-1}$ .

5  
6 We investigated the relationship between the incidence of deep convective clouds,  
7 INPs, and  $N_i$  at all grid points over the TP based on the different formation  
8 mechanisms of cirrus clouds. As shown in Fig. 2a, deep convection occurrences  
9 (DCO) is significantly higher in the southern and southeastern regions of the Plateau,  
10 where the  $N_i$  tend to be elevated (Fig. 1). Also,  $N_i$  revealed a positive nonlinear  
11 relationship with DCO, with a coefficient of determination ( $R^2$ ) of 0.55 ( $p < 0.01$ ) and a  
12 root mean square error (RMSE) of  $24.03 \text{ L}^{-1}$ , indicating that deep convective activity  
13 plays a significant role in modulating  $N_i$  over the TP. During the ASM, frequent deep  
14 convection in the southern TP facilitates the transport of warm, moist air and water  
15 droplets from the Indian Ocean and the Bay of Bengal to higher altitudes (He et al.,  
16 2019). Under moist conditions, ascending air parcels are more likely to experience a  
17 prolonged period of ice supersaturation, thereby increasing the probability of  
18 exceeding the supersaturation threshold required for homogeneous ice nucleation. In  
19 humid environments, air parcels can therefore maintain supersaturated conditions for  
20 a longer duration, making homogeneous nucleation more likely to dominate under  
21 such circumstances (Zhao et al., 2018). By contrast, heterogeneous nucleation is  
22 initiated by INPs and typically requires a lower ice supersaturation threshold,  
23 allowing it to occur earlier during ascent (DeMott et al., 2010). As a result, in  
24 environments with abundant water vapor, homogeneous nucleation may gain a

1 relative advantage in competition with heterogeneous nucleation, favouring the  
2 formation of higher  $N_i$ .

3 This interpretation is consistent with the relatively high  $N_i$  observed over the  
4 southern TP during summer. However, within an observational framework alone, the  
5 respective contributions of dynamical conditions, aerosol properties, and  
6 thermodynamic processes cannot be fully disentangled. The interpretation presented  
7 here should therefore be regarded as a qualitative explanation based on physical  
8 consistency rather than a definitive attribution.

9 In addition to convective activity, the presence of INPs also plays a critical role in  
10 modulating  $N_i$  over the TP. Zhao et al. (2018), using nine years of satellite  
11 observations, demonstrated that ice crystal formation is regulated not only by the  
12 availability of INPs but also by ambient water vapor conditions. This highlights the  
13 important role of moisture as a prerequisite for cirrus cloud evolution, while  
14 emphasizing that high water vapour availability alone is not sufficient to guarantee ice  
15 formation. Ice nucleation can only occur when the ice saturation ratio exceeds the  
16 threshold required for freezing; without reaching this threshold, no ice formation is  
17 possible (Gettelman et al., 2010). As a result, moisture should be regarded as a  
18 necessary background condition rather than a direct or sufficient driver of ice crystal  
19 formation.

20 Consequently, when investigating the relationship between INPs and  $N_i$ , directly  
21 comparing INPs and  $N_i$  across all grid cells may lead to misleading interpretations.  
22 This is because differing atmospheric conditions, particularly variations in moisture  
23 and the development of ice supersaturation, can strongly influence whether ice  
24 formation occurs. For example, high  $N_i$  in one grid cell may primarily reflect  
25 favourable moisture conditions that allow supersaturation to be achieved, rather than  
26 an enhanced influence of INPs, whereas in another grid cell the potential effect of  
27 INPs may be masked if the supersaturation threshold is not exceeded.

28 In principle, restricting the analysis to grid cells with broadly similar atmospheric  
29 conditions would allow a more direct comparison. However, the TP exhibits  
30 pronounced spatial heterogeneity, especially between its northern and southern

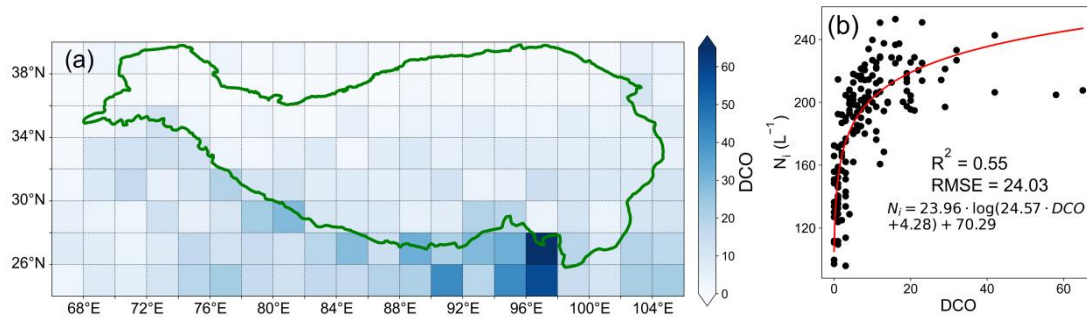
1 regions. To partially account for differences in moisture-related thermodynamic  
 2 conditions, this study introduces the IWC confined INPs concentration (ICIC),  
 3 defined as the logarithm of the ratio between the occurrence number of smoke (or dust)  
 4 particles and IWC within each grid cell (Eq. 3). By standardization, this metric  
 5 improves the comparability of the analysis to some extent. To further demonstrate the  
 6 robustness of this normalization, we compute the partial correlation between INPs and  
 7  $N_i$  after removing the effect of IWC. The resulting coefficient,  $r = -0.38$ , confirms that  
 8 the ICIC formulation effectively reduces moisture-related confounding.

$$9 \quad ICIC (type) = \log \left( \frac{type_{event}}{IWC} \right) \quad (3)$$

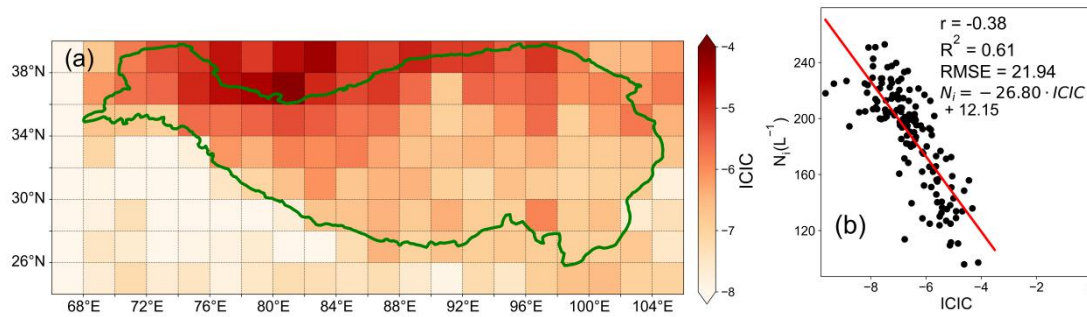
10 Where *type* is dust or smoke,  $type_{event}$  is the number of events of that aerosol type,  
 11 and  $ICIC(type)$  is the ICIC value corresponding to that aerosol type in the  
 12 corresponding grid.

13 Fig.3a shows the spatial distribution of this metric, revealing that ICIC is  
 14 predominantly concentrated in the northern part of the Plateau, with significantly  
 15 lower values in the south. Moreover, an inverse nonlinear relationship is observed  
 16 between ICIC and  $N_i$ , with a coefficient of determination ( $R^2$ ) of 0.61 ( $p < 0.01$ ) and a  
 17 root mean square error (RMSE) of  $22 \text{ L}^{-1}$ , indicates that the quantity of ICIC has a  
 18 significant impact on the  $N_i$  over the TP. While the  $N_i$  mainly arises from  
 19 homogenization nucleation, heterogeneous nucleation of INPs promotes the formation  
 20 of ice crystals (Khvorostyanov et al., 2006; DeMott et al., 2010) by absorbing a large  
 21 amount of water vapor and destroying the conditions for homogeneous nucleation.  
 22 The inhibitory effect of heterogeneous nucleation on homogeneous nucleation  
 23 becomes more pronounced with an increase in INPs content, leading to a lower  $N_i$ .  
 24 These two factors, namely the increased convective cloud frequency in the south and  
 25 the elevated INPs levels in the north, are the primary contributors to the observed  
 26 spatial pattern of  $N_i$ , which tends to be higher in the south and lower in the north.

27



1  
2 **Fig. 2. (a)** Horizontal distribution of DCO and **(b)** the relationship with  $N_i$  during the summer  
3 from 2006 to 2016 (except 2011) over the TP.



4  
5 **Fig. 3. (a)** Horizontal distribution of the ICIC and **(b)** the relationship with  $N_i$  during the summer  
6 from 2006 to 2016 (except 2011) over the TP.  $r(-0.38)$  in this figure is the partial correlation  
7 coefficient between INPs and  $N_i$  after removing the effect of IWC.

8

### 9 **3.2 Generation mechanism of ice crystal formation**

#### 10 **3.2.1 Contribution of the homogeneous nucleation**

11 Due to the condensation growth of cirrus cloud ice crystals in the upper  
12 atmosphere after nucleation, the observed ice crystal particle size in the satellite  
13 observation dataset only represents the post-growth effect, rendering it impossible to  
14 distinguish the contribution of different nucleation mechanisms to ice crystal size.  
15 Thus, this study considered the contribution of different nucleation mechanisms to the  
16 formation of cirrus cloud ice crystals by examining changes in the  $N_i$ .

17  $N_i$  for each vertical layer is calculated using Eq. (2), and Fig. 4 depicts the vertical  
18 distribution of the  $N_i$  from satellite observations and homogeneous nucleation. In  
19 cases where CALIOP does not indicate the presence of dust or smoke and the aerosol  
20 type is classified as ‘clean’, ice formation is assumed to occur via homogeneous  
21 freezing.

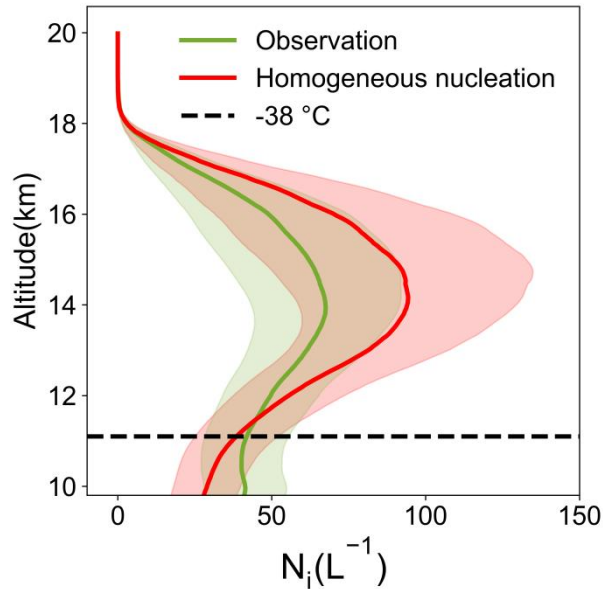
1 The satellite observations indicate that the  $N_i$  initially slowly increases with  
2 height and reaches its maximum of  $68 \text{ L}^{-1}$  at 14 km, and follows a decreasing trend  
3 with height up to 19 km. The vertical variation of  $N_i$  from homogeneous nucleation  
4 and observation both show an overall 'V' shaped distribution. However,  $N_i$  derived  
5 from homogeneous nucleation is consistently higher than the satellite observations at  
6 corresponding altitudes. Specifically, the number concentration from homogeneous  
7 nucleation peaks at 14 km with a value of  $94 \text{ L}^{-1}$ , which coincides with the altitude of  
8 the observed peak.

9 It is widely accepted that the formation of larger ice crystals through  
10 heterogeneous nucleation processes takes precedence over homogeneous nucleation  
11 (Shi et al., 2017; Barahona and Nenes, 2009). In fact, heterogeneous nucleation is the  
12 dominant ice formation mechanism at temperatures above  $-38 \text{ }^\circ\text{C}$ , whereas  
13 homogeneous nucleation occurs only when the temperature drops below  $-38 \text{ }^\circ\text{C}$  and  
14 when there are no INPs. Although homogeneous nucleation is the major contributor to  
15 the  $N_i$  (Cantrell and Heymsfield, 2005), heterogeneous nucleation has lower activation  
16 requirements and may occur earlier, potentially consuming water vapor and  
17 influencing subsequent ice formation. Under this interpretation, the observed  $N_i$  being  
18 lower than that expected under conditions favorable for homogeneous freezing could  
19 be consistent with the influence of heterogeneous nucleation. However, alternative  
20 explanations cannot be excluded. For example, lower  $N_i$  may also reflect weaker or  
21 less frequent updrafts, which would limit the development of high ice supersaturation,  
22 or differences in cloud origin, such as a predominance of in-situ cirrus with limited  
23 contribution from liquid-origin ice detrained from deep convective updrafts  
24 (Gryspeerd et al., 2018; Lyu et al., 2025).

25 Additionally, it is also worth noting that the observed  $N_i$  slightly exceeds the  
26 values from homogeneous nucleation below approximately 12 km. This is likely  
27 because homogeneous nucleation has not yet become dominant in this layer, while the  
28 observed  $N_i$  reflects prior heterogeneous nucleation events that produced a relatively  
29 large number of ice crystals. Once homogeneous nucleation becomes active with  
30 decreasing temperature, it rapidly generates a substantially higher  $N_i$  than observed.

1 From a trend perspective, the 'V' shape vertical distribution and the peak position of  
2  $N_i$  is determined by the role of homogeneous nucleation, while the specific values at  
3 different altitudes are determined by the combined effect of homogeneous nucleation  
4 and heterogeneous nucleation.

5



6

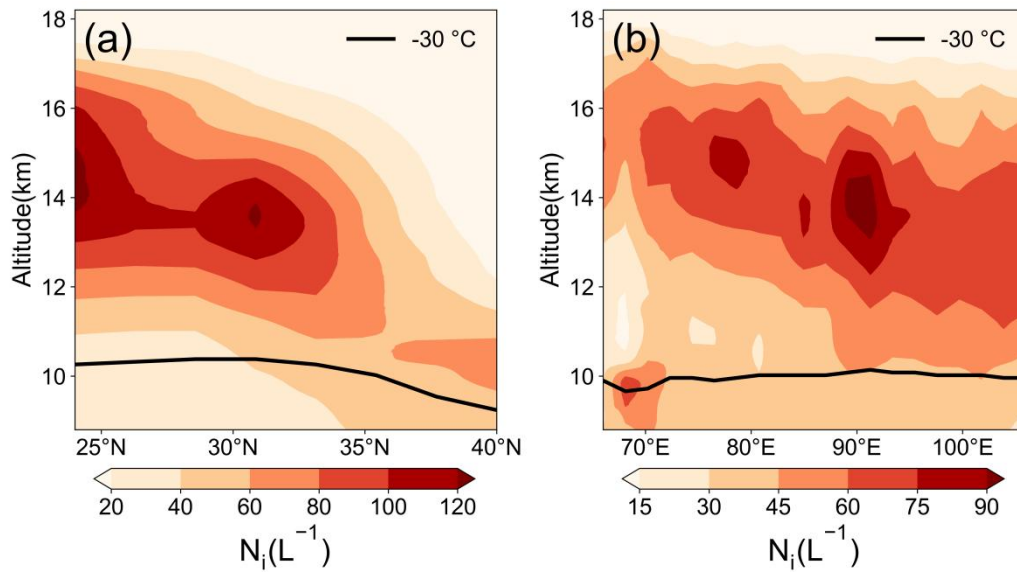
7 **Fig. 4.** Vertical profiles of observed and homogeneously nucleated  $N_i$ , with light shading  
8 indicating the standard error range.

9

10 To further investigate the vertical distribution characteristics of  $N_i$ , this study  
11 analyzes its spatial distribution across different latitudes and longitudes based on Fig.  
12 5. In the zonal cross-section (Fig. 5a), the  $N_i$  exhibits a pronounced maximum near 14  
13 km altitude between 28°N and 33°N, exceeding 120  $L^{-1}$ . Additionally, in the  
14 meridional cross-section (Fig. 5b), a peak  $N_i$  of over 90  $L^{-1}$  is observed near 90°E, also  
15 centered at 14 km altitude.

16 Together, these zonal and meridional distributions reveal a consistent vertical  
17 structure, with peak  $N_i$  occurring near 14 km, which could be influenced by  
18 homogeneous nucleation processes that dominate at these altitudes (Fig. 4). In  
19 contrast,  $N_i$  exhibits significant variability across both latitudinal and longitudinal  
20 directions, which may be related to the spatial distribution of water vapor and certain  
21 meteorological factors, such as vertical wind velocity, providing a foundation for the

1 subsequent analysis in this study.



2

3 **Fig. 5.** (a) The zonal distribution of  $N_i$  from 86 to 102°E for each latitude and (b) the meridional  
4 distribution of  $N_i$  from 24 to 40°N for each longitude.

5

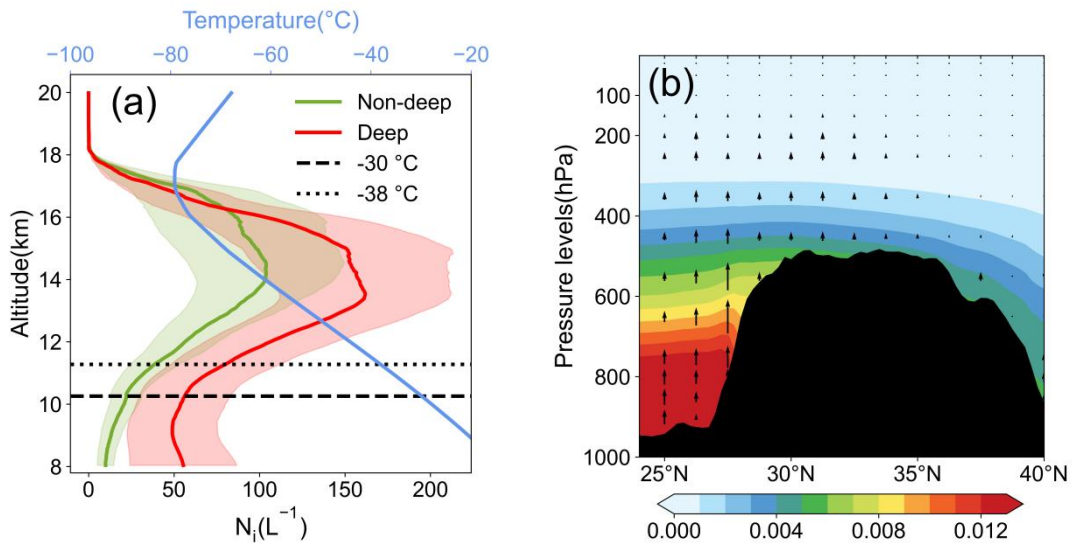
### 6 3.2.2 The effect of deep convective activity

7 In addition to homogeneous nucleation, deep convective cloud anvils are another  
8 significant source of ice crystal formation in the atmosphere. Fig. 6a compares the  
9 altitude-averaged  $N_i$  under different deep convective cloud conditions, based on all  
10 grid points across the TP where the incidence of deep convection exceeds 5% (Fig.  
11 2a). These selected regions represent areas with relatively frequent convective  
12 activity.

13 During summer, the tropopause height over the Tibetan Plateau typically ranges  
14 from about 16 - 18 km (Sun et al., 2021), providing an important vertical reference for  
15 cirrus cloud development. The top of cirrus clouds can develop near 18 km with a  
16 relatively low  $N_i$  for the case of non-deep convection activity, and at 14 km, reaches  
17 its peak of 104  $L^{-1}$ . When deep convection activity occurs, the  $N_i$  at the same altitude  
18 is significantly higher, and at 14 km, reaches its peak of 162  $L^{-1}$ . During summer,  
19 strong upward motions over the southern TP can transport both moist air and  
20 pre-existing ice crystals from the lower troposphere (below 12 km) into the upper  
21 troposphere via convective outflow anvils. These processes may create favorable

1 conditions for enhanced  $N_i$ , while homogeneous nucleation may additionally occur  
 2 under sufficiently cold and supersaturated conditions. It is therefore suggested that the  
 3 observed  $N_i$  peak near 14 km is associated with the combined effects of convective  
 4 transport, dynamical accumulation, and ice formation processes. At 14 km ( about 140  
 5 hPa), where the vertical wind speed is nearly zero,  $N_i$  accumulates significantly above  
 6 this level, while a substantial amount is transported upward from below 14 km. This  
 7 upward transport, combined with the accumulation, results in the peak at 14 km (Fig.  
 8 4b). Satellite observations also indicate that during the development of deep  
 9 convective clouds, approximately 95% of the cloud tops are located at or below 16 km.  
 10 This vertical distribution suggests that the influence of deep convection is mainly  
 11 confined below 16 km. Consequently,  $N_i$  above this level remains relatively  
 12 unchanged, indicating limited impact from convective processes at higher altitudes.

13



14

15 **Fig. 6.** (a) Vertical profile of the  $N_i$  affected by DCO and (b) the zonal distribution of vertical  
 16 winds averaged from 86 to 102°E for each latitude. The contour is specific humidity ( $kg\ kg^{-1}$ ).

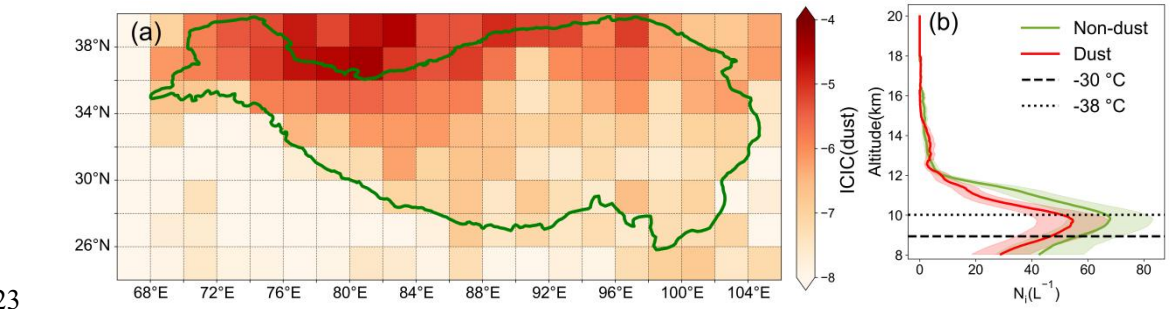
17

### 18 3.2.3 Heterogeneous nucleation effect of INPs

19 In the northern part of the TP, convective activity is relatively weak, but dust  
 20 aerosol content is high (Fig. 7a). The increase in  $N_i$  is primarily attributed to  
 21 heterogeneous nucleation induced by INPs. Considering the frequent dust activity in

1 this region, we selected grid points with ICIC(dust) greater than -5 as the primary  
 2 study area. These grid points are predominantly located in the northern Plateau,  
 3 adjacent to Xinjiang, a typical semi-arid region characterized by abundant dust  
 4 aerosols. These dust particles facilitate water vapor adsorption in the lower  
 5 atmosphere and promote ice crystal formation through heterogeneous nucleation  
 6 (Huang et al., 2021; Hoose and Möhler, 2012).

7 Fig. 7b illustrates the effect of dust aerosol particles on  $N_i$  in this area. The results  
 8 suggest that the presence of dust is associated with a reduction of  $N_i$  in cirrus clouds,  
 9 with concentrations above 12 km becoming very small. During non-dust periods,  
 10 although INPs remain present, their activation efficiency may be relatively high,  
 11 allowing a large fraction of aerosol ice nuclei to be activated, resulting in weaker  
 12 suppression of ice crystal formation. In contrast, elevated dust concentrations in the  
 13 lower atmosphere may enhance heterogeneous nucleation, thereby consuming  
 14 available water vapor and potentially inhibiting additional ice crystal formation,  
 15 which could lead to a reduction of  $N_i$ . Within this interpretative framework,  $N_i$  during  
 16 non-dust periods tends to be higher than during dust conditions. However, due to  
 17 limited water vapor in this region, a large fraction of moisture may already be  
 18 depleted in the lower atmosphere, which could contribute to very low  $N_i$  above 12 km.  
 19 Consequently, the suppressive effect of heterogeneous nucleation may limit ice crystal  
 20 formation through homogeneous nucleation at higher altitudes, making cirrus cloud  
 21 development more difficult in these upper layers. In regions with low water vapor  
 22 content, INPs may play an important role in modulating  $N_i$ .



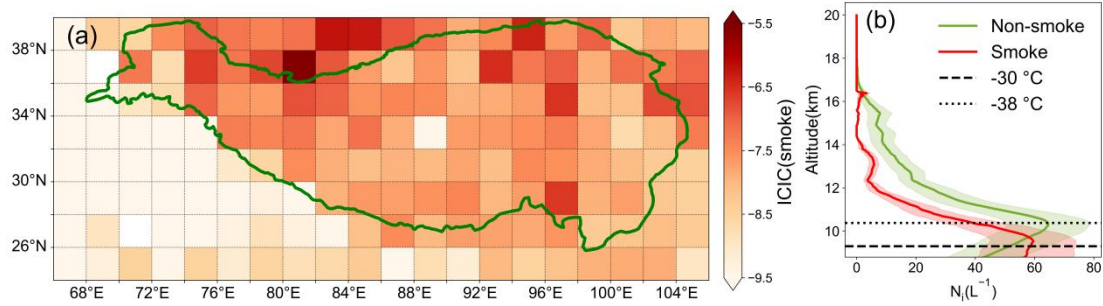
23 **Fig. 7. (a)** Horizontal distribution of ICIC(dust) and **(b)** the vertical profile of the  $N_i$  affected by  
 24 dust and non-dust events.  
 25

1

2 Besides dust aerosol, smoke aerosol particles generated by human activities are  
3 considered another potential source of heterogeneous nucleation for cirrus clouds over  
4 the TP. In this research, grid points with ICIC(smoke) greater than  $-6.5$  were selected  
5 as the primary research region to examine the possible influence of smoke INPs on  $N_i$   
6 (Fig. 8a).

7 It is observed that the presence of smoke aerosols is associated with a decrease in  
8  $N_i$ , with the maximum vertical extent of cirrus clouds limited to around 14 km (Fig.  
9 8b). One possible interpretation is that, during smoke events, ice crystal formation in  
10 the lower atmosphere may be influenced by smoke-derived INPs, under which  
11 heterogeneous nucleation could become more active. The relatively high abundance  
12 of smoke INPs may enhance competition among ice particles, potentially suppressing  
13 additional ice crystal formation and resulting in lower  $N_i$  compared to non-smoke  
14 conditions. In this hypothetical framework, smoke INPs may be efficiently activated  
15 through heterogeneous nucleation, while any remaining water vapor could still  
16 contribute to ice formation via homogeneous nucleation. From this perspective,  $N_i$   
17 tends to be higher during non-smoke periods, when fewer INPs may lead to weaker  
18 suppression effects. However, due to the inherently low water vapor content in this  
19 region, the vertical development of cirrus clouds appears to be constrained, and even  
20 during non-smoke periods, the maximum cloud height remains limited to  
21 approximately 17 km.

22 Homogeneous nucleation is often associated with a peak in  $N_i$  near 14 km.  
23 However, under dust and smoke conditions, such a peak is not clearly observed. One  
24 possible explanation is that dust and smoke aerosols are mainly concentrated over the  
25 northern TP, where the vertical wind speed around 400 hPa is relatively weak (Fig.  
26 6b). Reduced vertical transport may limit the upward redistribution of ice crystals,  
27 thereby influencing the vertical structure of  $N_i$ .



1  
2 **Fig. 8. (a)** Horizontal distribution of ICIC(smoke) and **(b)** the vertical profile of the  $N_i$  affected by  
3 smoke and non-smoke events.

#### 5 **4 Conclusion**

6 This study analyzed the distribution characteristics and formation mechanism of  
7 cirrus cloud ice crystals during the summer of 2006 to 2016 (except 2011) over the TP,  
8 mainly using DARDAR-Nice data combined with aerosol product data.

9 The main conclusions are summarized as follows: (1)  $N_i$  shows pronounced  
10 spatial variability across the TP, with generally higher values over the southern TP  
11 than over the northern TP. This contrast is statistically associated with differences in  
12 large-scale meteorological conditions, including more frequent deep convection over  
13 the southern TP, whereas the northern TP is characterized by more frequent aerosol  
14 occurrence and lower  $N_i$ .

15 (2) The vertical distribution of  $N_i$  exhibits a characteristic V-shaped structure,  
16 consistent with statistical signatures expected under conditions favorable for  
17 homogeneous freezing. The values of  $N_i$  at varying altitudes are likely determined by  
18 the combined effects of both homogeneous and heterogeneous nucleation.

19 (3) Regions influenced by deep convection tend to exhibit higher  $N_i$  at a given  
20 altitude than non-convective regions. This behavior is consistent with the role of  
21 convective outflow anvils in transporting moisture and pre-existing ice crystals into  
22 the upper troposphere, while homogeneous freezing may additionally occur under  
23 sufficiently cold and supersaturated conditions.

24 (4) Under dust and smoke influenced conditions, ice formation in the lower  
25 atmosphere is statistically associated with heterogeneous nucleation occurring prior to

1 homogeneous freezing, and  $N_i$  is generally lower than non-dust(smoke) conditions.  
2 This behavior may be related to early vapor consumption, differences in vertical  
3 motion, and sedimentation effects. These interpretations represent one possible  
4 explanation of the observed.

5 Several limitations should be noted. This study integrates several validated  
6 satellite retrieval products in the analysis. Nevertheless, differences in retrieval  
7 methodologies and sensor sensitivities among these products introduce inherent  
8 uncertainties, which may affect the quantitative interpretation of the results to some  
9 extent. In addition, the use of multi-year climatological averages smooths event-scale  
10 extremes associated with strong updrafts or short-lived dynamical processes. Aerosol  
11 information represents grid-cell-scale and climatological conditions rather than  
12 instantaneous cloud–aerosol interactions. Consequently, the results should be regarded  
13 as hypothesis-driven and exploratory, providing statistical context and motivation for  
14 future studies combining satellite observations, in-situ measurements, and modeling.

15

16 *Acknowledgements.* This study was supported by the National Natural Science Foundation of China  
17 (NSFC, Grant Numbers: 42330603), the Open Research of Key Laboratory of Intelligent  
18 Meteorological Observation Technology in China Meteorological Administration (ZNGC2024ZD02),  
19 the Science and Technology Planning Program of Xinjiang (2022E01047), National Natural Science  
20 Foundation of China (42030612 and 42175179), and the Natural Science Foundation of Shanghai  
21 (22ZR1404000). The authors gratefully acknowledge the ECMWF for providing ERA5 data, and the  
22 NASA for providing CloudSat and CALIPSO data. In addition, the DARDAR-Nice product used in  
23 this study was obtained from the AERIS/ICARE data center.

24

## 25 **References**

26 Ansmann, A., Jimenez, C., Knopf, D. A., Roschke, J., Bühl, J., Ohneiser, K., and Engelmann, R.: Impact of  
27 wildfire smoke on Arctic cirrus formation–Part 2: Simulation of MOSAiC 2019–2020 cases, *Atmos. Chem.*  
28 *Phys.*, 25, 4867–4884, 2025.

29 Austin, R. T., Heymsfield, A. J., and Stephens, G. L.: Retrieval of ice cloud microphysical parameters using the  
30 CloudSat millimeter-wave radar and temperature, *J. Geophys. Res.*, 114, doi:10.1029/2008JD010049, 2009.

31 Austin, R. T.: Level 2B radar-only cloud water content (2B-CWC-RO) process description document, Data  
32 Processing Center, 24, 2007.

33 Barahona, D. and Nenes, A.: Parameterizing the competition between homogeneous and heterogeneous freezing in

1 ice cloud formation-polydisperse ice nuclei, *Atmos. Chem. Phys.*, 9, 5933-5948, 2009.

2 Baran, A. J.: From the single-scattering properties of ice crystals to climate prediction: A way forward, *Atmos. Res.*,  
3 112, 45-69, 2012.

4 Cairo, F., Krämer, M., Afchine, A., Di Donfrancesco, G., Di Liberto, L., Khaykin, S., Lucaferri, L., Mitev, V., Port,  
5 M., Rolf, C., Snels, M., Spelten, N., Weigel, R., and Borrmann, S.: A comparative analysis of in situ  
6 measurements of high-altitude cirrus in the tropics, *Atmos. Meas. Tech.*, 16, 4899-4925, 2023.

7 Cantrell, W. and Heymsfield, A.: Production of ice in tropospheric clouds: A review, *Bull. Am. Meteorol. Soc.*, 86,  
8 795-808, 2005.

9 Chen, B. and Liu, X.: Seasonal migration of cirrus clouds over the Asian Monsoon regions and the Tibetan Plateau  
10 measured from MODIS/Terra, *Geophys. Res. Lett.*, 32, doi:1029/2004GL020868, 2005.

11 Chen, Q. L., Gao, G. L., Li, Y., Cai, H. K., Zhou, X., and Wang, Z. L.: Main detrainment height of deep convection  
12 systems over the Tibetan Plateau and its southern slope, *Adv. Atmos. Sci.*, 36, 1078-1088, 2019.

13 Chen, Y., DeMott, P. J., Kreidenweis, S. M., Rogers, D. C., and Sherman, D. E.: Ice formation by sulfate and  
14 sulfuric acid aerosol particles under upper-tropospheric conditions, *J. Atmos. Sci.*, 57, 3752-3766, 2000.

15 Comstock, J. M., Lin, R. F., Starr, D. O. C., and Yang, P.: Understanding ice supersaturation, particle growth, and  
16 number concentration in cirrus clouds, *J. Geophys. Res. Atmos.*, 113, D23211, 2008.

17 Delanoë, J., and Hogan, R. J.: A variational scheme for retrieving ice cloud properties from combined radar, lidar,  
18 and infrared radiometer, *J. Geophys. Res.*, 113, D07204, 2008.

19 Delanoë, J., and Hogan, R. J.: Combined CloudSat-CALIPSO-MODIS retrievals of the properties of ice clouds, *J.*  
20 *Geophys. Res.*, 115, D00H29, 2010.

21 DeMott, P. J., Prenni, A. J., Liu, X., Kreidenweis, S. M., Petters, M. D., Twohy, C. H., Richardson, M., Eidhammer,  
22 T., and Rogers, D.: Predicting global atmospheric ice nuclei distributions and their impacts on climate, *Proc.*  
23 *Natl. Acad. Sci.*, 107, 11217-11222, 2010.

24 Duft, D., and Leisner, T.: Laboratory evidence for volume-dominated nucleation of ice in supercooled water  
25 microdroplets, *Atmos. Chem. Phys.*, 4, 1997-2000, 2004.

26 Fan, F., Zhang, S., Peng, Z., Chen, J., Su, M., Moghtaderi, B., and Doroodchi, E.: Numerical investigation of  
27 heterogeneous nucleation of water vapour on PM10 for particulate abatement, *Can. J. Chem. Eng.*, 97,  
28 930-939, 2019.

29 Fu, R., Hu, Y., Wright, J. S., Jiang, J. H., Dickinson, R. E., Chen, M., Filipiak, M., Read, W. G., Waters, J. W., and  
30 Wu, D. L.: Short circuit of water vapor and polluted air to the global stratosphere by convective transport over

1 the Tibetan Plateau, *Proc. Natl. Acad. Sci.*, 103, 5664-5669, 2006.

2 Gao, B. C., Yang, P., Guo, G., Park, S. K., Wiscombe, W. J., and Chen, B.: Measurements of water vapor and high  
3 clouds over the Tibetan Plateau with the Terra MODIS instrument, *IEEE Trans. Geosci. Remote Sens.*, 41,  
4 895-900, 2003.

5 Gettelman, A., Liu, X., Ghan, S. J., Morrison, H., Park, S., Conley, A. J., Klein, S. A., Boyle, J., Mitchell, D. L.,  
6 and Li, J. L.: Global simulations of ice nucleation and ice supersaturation with an improved cloud scheme in  
7 the Community Atmosphere Model, *J. Geophys. Res. Atmos.*, 115, 2010.

8 Gryspeerd, E., Sourdeval, O., Quaas, J., Delanoë, J., Krämer, M., and Kühne, P.: Ice crystal number concentration  
9 estimates from lidar-radar satellite remote sensing-Part 2: Controls on the ice crystal number concentration,  
10 *Atmos. Chem. Phys.*, 18, 14351-14370, 2018.

11 Guignard, A., Stubenrauch, C., Baran, A., and Armante, R.: Bulk microphysical properties of semi transparent  
12 cirrus from AIRS: a six years global climatology and statistical analysis in synergy with CALIPSO and  
13 CloudSat, *Atmos. Chem. Phys. Discuss.*, 11, doi:10.5194/acpd-11-24671-2011, 2011.

14 He, Q., Zheng, X., Li, J., Gao, W., Wang, Y., Cheng, T., Pu, J., Liu, J., and Li, C.: The role of ASM on the  
15 formation and properties of cirrus clouds over the Tibetan Plateau. *Tellus, Ser. B: Chem. Phys. Meteorol.*,  
16 71(1), 1577070.

17 Hendricks, J., Kärcher, B., and Lohmann, U.: Effects of ice nuclei on cirrus clouds in a global climate model, *J.*  
18 *Geophys. Res. Atmos.*, 116, D18206, 2011.

19 Hoose, C. and Möhler, O.: Heterogeneous ice nucleation on atmospheric aerosols: a review of results from  
20 laboratory experiments, *Atmos. Chem. Phys.*, 12, 9817-9854, 2012.

21 Hoose, C., and Möhler, O.: Heterogeneous ice nucleation on atmospheric aerosols: a review of results from  
22 laboratory experiments, *Atmos. Chem. Phys.*, 12, 9817-9854, 2012.

23 Huang, J. P., Liu, Y. Z., Wang, T. H., Yan, H. R., Li, J. M., and He, Y. L.: An overview of the aerosol and cloud  
24 properties and water vapor budget over the Qinghai-Xizang Plateau, *Plateau Meteorol.*, 40, 1225-1240, 2021.

25 Jin, L. J., Yin, Y., Wang, P. X., and Chen, B. J.: Numerical modeling of tropical deep convective anvil and  
26 sensitivity test on its response to changes in the cloud condensation nuclei concentration, *Chinese J. Atmos.*  
27 *Sci.*, 31, 793-804, 2007.

28 Kärcher, B. and Lohmann, U.: A parameterization of cirrus cloud formation: Heterogeneous freezing, *J. Geophys.*  
29 *Res. Atmos.*, 108, doi:10.1029/2002JD003220, 2003.

1 Kay, J. E. and Wood, R.: Timescale analysis of aerosol sensitivity during homogeneous freezing and implications  
2 for upper tropospheric water vapor budgets, *Geophys. Res. Lett.*, 35, L10809, 2008.

3 Khain, A., Ovtchinnikov, M., Pinsky, M., Pokrovsky, A., and Krugliak, H.: Notes on the state-of-the-art numerical  
4 modeling of cloud microphysics, *Atmos. Res.*, 55, 159-224, 2000.

5 Khvorostyanov, V. I., Morrison, H., Curry, J. A., Baumgardner, D., and Lawson, P.: High supersaturation and  
6 modes of ice nucleation in thin tropopause cirrus: Simulation of the 13 July 2002 Cirrus Regional Study of  
7 Tropical Anvils and Cirrus Layers case, *J. Geophys. Res. Atmos.*, 111, doi:10.1029/2004JD005235, 2006.

8 Kienast-Sjögren, E., Rolf, C., Seifert, P., Krieger, U. K., Luo, B. P., Krämer, M., and Peter, T.: Climatological and  
9 radiative properties of midlatitude cirrus clouds derived by automatic evaluation of lidar measurements,  
10 *Atmos. Chem. Phys.*, 16, 7605-7621, 2016.

11 Kim, M. H., Omar, A. H., Tackett, J. L., Vaughan, M. A., Winker, D. M., Trepte, C. R., Hu, Y. X., Liu, Z. Y., Poole,  
12 L. R., Pitts, M. C., Kar, J., and Magill, B. E.: The CALIPSO version 4 automated aerosol classification and  
13 lidar ratio selection algorithm, *Atmo. Meas. Tech.*, 11, 6107-6135, 2018.

14 Koop, T., and Murray, B.J.: A physically constrained classical description of the homogeneous nucleation of ice in  
15 water, *J. Chem. Phys.*, 145, 211915-1-211915-11, 2016.

16 Ladino Moreno, L. A., Stetzer, O., and Lohmann, U.: Contact freezing: a review of experimental studies, *Atmos.*  
17 *Chem. Phys.*, 13, 9745-9769, 2013.

18 Li, Q., Jiang, J. H., Wu, D. L., Read, W. G., Livesey, N. J., Waters, J. W., Zhang, Y., Wang, B., Filipiak, M. J., and  
19 Davis, C. P.: Convective outflow of South Asian pollution: A global CTM simulation compared with EOS  
20 MLS observations, *Geophys. Res. Lett.*, 32, doi:10.1029/2005GL022765, 2005.

21 Liu, Z., Omar, A., Vaughan, M., Hair, J., Kittaka, C., Hu, Y. X., Powell, K., Trepte, C., Winker, D., Hostetler, C.,  
22 Ferrare, R., and Pierce, R.: CALIPSO lidar observations of the optical properties of Saharan dust: A case  
23 study of long-range transport, *J. Geophys. Res. Atmos.*, 113, doi: 10.1029/2007JD008878, 2008.

24 Lyu, K., Liu, X., and Kärcher, B.: Exploring sources of ice crystals in cirrus clouds: comparative analysis of two  
25 ice nucleation schemes in CAM6, *Atmos. Chem. Phys.*, 25, 15369-15388, 2025.

26 Maeda, N.: Brief overview of ice nucleation. *Molecules*, 26, 392, 2021.

27 Mamouri, R. E., Ansmann, A., Ohneiser, K., Knopf, D. A., Nisantzi, A., Bühl, J., Engelmann, R., Skupin, A.,  
28 Seifert, P., Baars, H., Ene, D., Wandinger, U., and Hadjimitsis, D.: Wildfire smoke triggers cirrus formation:  
29 lidar observations over the eastern Mediterranean, *Atmos. Chem. Phys.*, 23, 14097-14114, 2023.

1 Mao, F., Shi, R., Rosenfeld, D., Pan, Z., Zang, L., Zhu, Y., and Lu, X.: Retrieving instantaneous extinction of  
2 aerosol undetected by the CALIPSO layer detection algorithm, *Atmos. Chem. Phys.*, 22(16), 10589-10602,  
3 2022.

4 McCluskey, C. S., DeMott, P. J., Prenni, A. J., Levin, E. J., McMeeking, G. R., Sullivan, A. P., Hill, T. C., Nakao,  
5 S., Carrico, C. M., and Kreidenweis, S. M.: Characteristics of atmospheric ice nucleating particles associated  
6 with biomass burning in the US: Prescribed burns and wildfires, *J. Geophys. Res. Atmos.*, 119, 10458-10470,  
7 2014.

8 Morris, C. E., Georgakopoulos, D. G., and Sands, D. C.: Ice nucleation active bacteria and their potential role in  
9 precipitation, *J. Phys. IV France.*, 121,87-103, 2004.

10 Murray, B. J., Broadley, S. L., Wilson, T. W., Bull, S. J., Wills, R. H., Christenson, H. K., Murray, E. J.: Kinetics of  
11 the homogeneous freezing of water, *Phys. Chem. Chem. Phys.*, 12, 10380–10387, 2010.

12 Murray, B. J., O'sullivan, D., Atkinson, J. D., and Webb, M. E.: Ice nucleation by particles immersed in  
13 supercooled cloud droplets, *Chem. Soc. Rev.*, 41, 6519-6554, 2012.

14 Murray, B. J., Wilson, T. W., Dobbie, S., Cui, Z., Al-Jumur, S. M., Möhler, O., Schnaiter, M., Wagner, R., Benz, S.,  
15 and Niemand, M.: Heterogeneous nucleation of ice particles on glassy aerosols under cirrus conditions, *Nat.*  
16 *Geosci.*, 3, 233-237, 2010.

17 Prabhakara, C., Kratz, D., Yoo, J.-M., Dalu, G., and Vernekar, A.: Optically thin cirrus clouds: Radiative impact on  
18 the warm pool, *J. Quant. Spectrosc. Radiat. Transfer.*, 49, 467-483, 1993.

19 Prenni, A. J., DeMott, P. J., Sullivan, A. P., Sullivan, R. C., Kreidenweis, S. M., and Rogers, D. C.: Biomass  
20 burning as a potential source for atmospheric ice nuclei: Western wildfires and prescribed burns, *Geophys. Res.*  
21 *Lett.*, 39, L11805, 2012.

22 Randel, W. J., Park, M., Emmons, L., Kinnison, D., Bernath, P., Walker, K. A., Boone, C., and Pumphrey, H.:  
23 Asian monsoon transport of pollution to the stratosphere, *Science*, 328, 611-613, 2010.

24 Shi, X. J., Zhu, S. P., Zhi, X. F., Du, K. Y., Liu, Q. G., and Wang, L. W.: Sensitivity study on three ice nucleation  
25 parameterizations, *Trans. Atmos. Sci.*, 40, 181-192, 2017.

26 Shi, X., Liu, X., and Zhang, K.: Effects of pre-existing ice crystals on cirrus clouds and comparison between  
27 different ice nucleation parameterizations with the Community Atmosphere Model (CAM5), *Atmos. Chem.*  
28 *Phys.*, 15, 1503-1520, 2015.

1 Sourdeval, O., Gryspeerdt, E., Krämer, M., Goren, T., Delanoë, J., Afchine, A., Hemmer, F., and Quaas, J.: Ice  
2 crystal number concentration estimates from lidar-radar satellite remote sensing-Part 1: Method and  
3 evaluation, *Atmos. Chem. Phys.*, 18, 14327-14350, 2018.

4 Stephens, G. L.: Cloud feedbacks in the climate system: A critical review, *J. Climate.*, 18, 237-273, 2005.

5 Sun, N., Fu, Y., Zhong, L., Zhao, C., & Li, R.: The impact of convective overshooting on the thermal structure over  
6 the Tibetan Plateau in summer based on TRMM, COSMIC, Radiosonde, and Reanalysis Data. *J. Climate*, 34,  
7 8047-8063, 2021.

8 Takahashi, H. and Luo, Z.: Where is the level of neutral buoyancy for deep convection? *Geophys. Res. Lett.*, 39,  
9 2012.

10 Wang, C. M., Ye, J. D. and Wei, S. Y.: A numerical experiment of aerosol concentration affecting warm rain  
11 process, *Scientia Meteor. Sinica*, 17, 316-323, 1997.

12 Wang, H. Q., and Zhao, G. X.: Cloud and Radiation-I: Cloud climatology and radiative effects of clouds, *Scientia*  
13 *Atmos. Sinica*, 18, 910-932, 1994.

14 Wang, K., Chen, J., Hong, Z. C., Yan, C. Q., and He, Q. S.: Research of the distribution characteristics and  
15 generation mechanism of cirrus clouds over the Qinghai-Xizang Plateau in summer, *Plateau Meteor.*, doi:10.  
16 7522/j. issn. 1000-0534. 2022. 00069, 2023.

17 Wang, P. H., Minnis, P., McCormick, M. P., Kent, G. S., and Skeens, K. M.: A 6-year climatology of cloud  
18 occurrence frequency from Stratospheric Aerosol and Gas Experiment II observations (1985-1990), *J.*  
19 *Geophys. Res. Atmos.*, 101, 29407-29429, 1996.

20 Xie, S. F., Wang, Y. J., Huang, L. K., Pan, Q. Y., and Wei, P. Z.: Accuracy analysis of Tm calculated by ERA5 and  
21 MERRA-2 reanalysis data over China, *J. Geo. Geodyn.*, 41, 771-776, 2021.

22 Xue, X. N, Deng, X. B., and Liu, G. H.: Study on characteristics of Qinghai-Tibetan Plateau cirrus based on  
23 satellite data, *Plateau Meteor.*, 37, 505-513, 2018.

24 Yang, Y. K., Zhao, C. F., and Fan, H.: Spatiotemporal distributions of cloud properties over China based on  
25 Himawari-8 advanced Himawari imager data, *Atmos. Res.*, 240, doi:10.1016/j.atmosres.2020.104927, 2020.

26 Zhang, F., Yu, Q. R., Mao, J. L., Dan, C., Wang, Y., He, Q., Cheng, T., Chen, C., Liu, D., and Gao, Y.: Possible  
27 mechanisms of summer cirrus clouds over the Tibetan Plateau, *Atmos. Chem. Phys.*, 20, 11799-11808, 2020.

28 Zhang, K., Liu, X., Wang, M., Comstock, J. M., Mitchell, D. L., Mishra, S., and Mace, G. G.: Evaluating and  
29 constraining ice cloud parameterizations in CAM5 using aircraft measurements from the SPARTICUS  
30 campaign, *Atmos. Chem. Phys.*, 13, 4963-4982, 2013.

- 1 Zhao, B., Liou, K. N., Gu, Y., Jiang, J. H., Li, Q., Fu, R., Huang, L., Liu, X., Shi, X., Su, H., and He, C.: Impact of  
2 aerosols on ice crystal size, *Atmos. Chem. Phys.*, 18, 1065-1078, 2018.
- 3 Zhao, C., Chen, Y., Li, J., Letu, H., Su, Y., Chen, T., and Wu, X.: Fifteen-year statistical analysis of cloud  
4 characteristics over China using Terra and Aqua Moderate Resolution Imaging Spectroradiometer  
5 observations, *Int. J. Climatol.*, 39, 2612-2629, 2019.
- 6 Zheng, J. Y., Liu, D., Wang, Z. E., Tian, X. M., Wang, Y. J., and Xie, C. B.: Global distribution and seasonal  
7 variation of clouds observed from CloudSat/CALIPSO, *Acta Meteor. Sinica.*, 76, 420-433, 2018.